Research Article Vol. 28, No. 18 / 31 August 2020 / *Optics Express* 26151

Optics EXPRESS

Liquid-crystal splitter for generating and separating autofocusing and autodefocusing circular Airy beams

BINGYAN WEI,[1,4,5] **YUAN ZHANG,**[1,4] **PENG LI,**[1] **SHENG LIU,**[1] **WEI HU,**[2] **YANQING LU,**[2] **YUNLONG WU,**[3] **XIANAN DOU,**[3] **AND JIANLIN ZHAO**[1,6]

[1] *MOE Key Laboratory of Material Physics and Chemistry under Extraordinary Conditions, and Shaanxi Key Laboratory of Optical Information Technology, School of Physical Science and Technology, Northwestern Polytechnical University, Xi'an 710129, China*
[2] *National Laboratory of Solid State Microstructures, College of Engineering and Applied Sciences, and Collaborative Innovation Center of Advanced Microstructures, Nanjing University, Nanjing 210093, China*
[3] *State Key Laboratory of Pulsed Power Laser Technology, National University of Defense Technology, Hefei 230037, China*
[4] *These authors contributed equally to this work*
[5] *wbyxz@nwpu.edu.cn*
[6] *jlzhao@nwpu.edu.cn*

Abstract: A unique splitter is proposed and demonstrated to realize the generation and separation of autofocusing and autodefocusing circular Airy beams (CABs). The design of the splitter is derived from the Fourier transform of a CAB associated with the Pancharatnam–Berry phase, and the fabrication is carried out via a liquid-crystal photo-patterning technique. Autofocusing and autodefocusing CABs of orthogonal circular polarization states are spatially diffracted under the modulation of the splitter, and the energy distribution between these two CABs can be controlled by the incident polarization. A focal length of 40 cm is obtained, which can be customized as required. The propagation dynamics of the generated autofocusing and autodefocusing CABs are investigated, and the experimental results are in good accordance with the corresponding simulations. The additional merits of the splitter, such as reconfigurability, tunability, high efficiency, and wide operating wavelength range, may motivate novel applications of CABs in the areas of laser optics, biomedicine, and modern displays.

1. Introduction

With the rapid development of optical communications technology, the beam splitter as a critical component has triggered extensive research. A beam splitter is a device that can split an incident beam into two or more beams. In addition to optical communication systems, beam splitters are also required for interferometers, autocorrelators, cameras, projectors, and displays, and even play an important role in quantum entanglement [1] and ghost imaging [2]. Another necessary capability of most of these applications is focusing or defocusing. Lenses are usually utilized to achieve this functionality, particularly those made of liquid crystals (LCs) [3–5]; the outstanding electro-optical tunability of LCs makes them excellent candidates for modern displays including augmented-reality [6,7], virtual-reality [8], 3D [9], and head-mounted [10] displays.

Another way to realize the focusing or defocusing phenomenon is to generate circular Airy beams (CABs) [11], which have also attracted attention in recent decades. A CAB can be regarded as an Airy beam [12] in cylindrical coordinates [11]. The intrinsic self-accelerating nature of the Airy beam endows the CAB with an autofocusing or autodefocusing characteristic [13]. More importantly, an autofocusing CAB maintains a relatively low intensity profile before

#400636 https://doi.org/10.1364/OE.400636
Journal © 2020 Received 19 Jun 2020; revised 31 Jul 2020; accepted 14 Aug 2020; published 20 Aug 2020

abruptly focusing its energy at the focal region. This peculiar feature is particularly preferable for medical treatments based on laser technology, in which only the target area must be irradiated with the surrounding tissue left intact [11]. CABs have also been widely studied in areas such as the manipulation of microparticles [13], generation of nonlinear intense light bullets [14] and other nonlinear processes including multiphoton absorption, stimulated Raman scattering, and optical filaments in gases [15]. However, most of the current studies mainly concentrate on the autofocusing feature of the CAB while little attention is paid to exploiting the opposite autodefocusing behavior. Moreover, to the best of our knowledge, there is still a lack of research on the beam splitter that can integrate the functions of generating, separating and modulating the autofocusing and autodefocusing CABs. The invention of such splitters will greatly facilitate the flexibility in the usage of CABs and expand their application ranges.

In this paper, by taking advantage of the properties of LCs, we demonstrate a unique splitter, the LC CAB splitter (CABS), for the generation and separation of autofocusing and autodefocusing CABs. The phase design of the LC CABS is derived from the Fourier transform (FT) of the CAB with the introduction of the Pancharatnam–Berry (PB) phase [16,17]. A digital-micro-mirror-device (DMD)-based microlithography system and SD1-based photoalignment technology [18] are utilized to fabricate the LC CABS. A focal length of 40 cm is obtained, which is customizable, and the separation distance between the autofocusing and autodefocusing CABs can be adjusted by re-exposing the LC sample due to the rewritability of SD1. Moreover, the energy distribution between the autofocusing and autodefocusing states can be controlled by varying the incident polarization. The proposed LC CABS may have potential applications in biomedical treatment, laser processing, and even the modern displays mentioned above.

2. Principles and experiments

Through asymptotic analysis, the FT of a CAB with amplitude $u(r) = \mathrm{Ai}(r_0 - r)\exp[a(r_0 - r)]$ can be expressed by [19]:

$$F(k) = (r_0 + k^2)e^{-ak^2}\sqrt{\frac{kr_0 + k^3/3}{kr_0 + k^3}}J_0(kr_0 + k^3/3) = G(k)J_0(kr_0 + k^3/3), \tag{1}$$

where $\mathrm{Ai}(\cdot)$ is the Airy function, r is the scaled polar coordinate, r_0 is related to the radius of the main ring, a is the apodization factor, the wave vector k is the Fourier spectrum coordinate, $J_0(\cdot)$ is the zero-order Bessel function, and $G(k)$ represents the complicated super-Gaussian envelope whose amplitude is modulated by a function that scales quadratically and apodized by a Gaussian function [19]. Regardless of the amplitude term, attentions should be focused on the phase term contained in the argument of the zero-order J_0 Bessel function whose linear phase is enhanced by a cubic term [19]. For the generation of zero-order Bessel beam, it can be realized by modulating the Gaussian beam through the conical (radial linear) phase optical element [20]. Therefore, as an analogy, one can generate an autofocusing CAB by modulating the Gaussian beam through the combination of a radial cubic phase and a radial linear phase, as shown in Figs. 1(a) and 1(b), respectively. To implement a splitter, a grating structure [21–23] as shown in Fig. 1(c) is appended. By superimposing these three phase structures, that is,

$$\varphi_{\mathrm{CABS}} = \beta\rho^3 + 2\pi\rho/d - 2\pi x/\Lambda, \tag{2}$$

the CABS phase design shown in Fig. 1(d) can thus be achieved. Herein, β is a parameter relating to the radial cubic phase modulation, $\rho = \mathrm{sqrt}(x^2 + y^2)$, d is the radial period of the radial linear phase, and Λ is the period of the grating structure. Considering the following fabrication equipment and taking a pixel as the unit, the designed parameters for d and Λ are 245.7 pixels and 40 pixels, respectively.

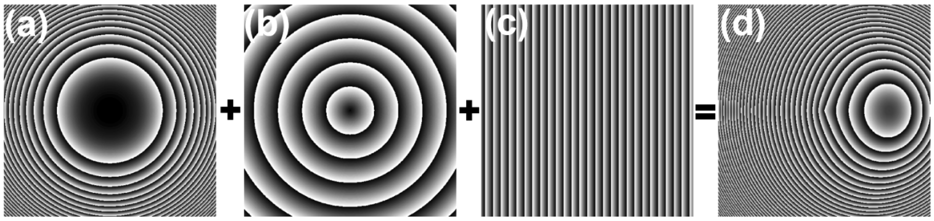

Fig. 1. Principle of the CABS phase design. (a) Radial cubic phase, (b) radial linear phase, (c) grating structure, and (d) the sum of the former three, i.e., the CABS phase. The gray level in these phase patterns from black to white indicates the phase value from 0 to 2π. However, when introduced by the PB phase, black to white can also be regarded as the optical axis varying from 0 to π.

Furthermore, the PB phase is also introduced owing to its merits of efficiently modulating optical waves and polarization controllability [24–30]. The amount of PB phase modulation depends on the orientation angle of the optical axis of the anisotropic medium, which is chosen to be nematic LC E7 in the following experiment. For spatially structured light beams with featured phase Φ, they can be easily realized by setting the orientation of the optical axis of the anisotropic medium as $\alpha = \Phi/2$ [30]. Herein, the orientation of LC directors is set to follow $\alpha = \varphi/2 = \rho^3/2 + \pi\rho/d$ - $\pi x/\Lambda$. Consequently, Fig. 1(d) can also be regarded as the director distribution of the LC CABS in which black to white corresponds to the orientation varying from 0 to π. The diffraction property of the LC CABS based on the PB phase modulation can be analyzed by Jones calculus. The Jones matrix for the LC CABS can be expressed as

$$\mathbf{M} = \cos\frac{\Gamma}{2}\begin{bmatrix} 1 & 0 \\ 0 & 1 \end{bmatrix} - i\sin\frac{\Gamma}{2}\begin{bmatrix} \cos 2\alpha & \sin 2\alpha \\ \sin 2\alpha & -\cos 2\alpha \end{bmatrix}, \tag{3}$$

where $\Gamma = 2\pi\Delta n d/\lambda$ is the phase retardation, Δn is the birefringence of the LC E7, d is the gap of the LC cell, and λ is the incident wavelength. As any polarized light can be regarded as the combination of two orthogonal circularly polarized light components, the following analyses are based on the incidence of circular polarization states. When a circularly polarized plane wave illuminates the LC CABS, the output electric field will be transformed into

$$\mathbf{E}_{\text{out}} = \mathbf{M}\cdot\mathbf{E}_{\text{in}} = \mathbf{M}\cdot\begin{bmatrix} 1 \\ \pm i \end{bmatrix} = \cos\frac{\Gamma}{2}\begin{bmatrix} 1 \\ \pm i \end{bmatrix} - i\sin\frac{\Gamma}{2}\exp[\pm i(\beta\rho^3 + 2\pi\rho/d)]\exp(\mp i2\pi x/\Lambda)\begin{bmatrix} 1 \\ \mp i \end{bmatrix}, \tag{4}$$

where $\mathbf{E}_{\text{in}} = [1, \pm i]^{\text{T}}$ represents the incident electric field, with (+) standing for left circular polarization (LCP) and (-) standing for right circular polarization (RCP). Specifically, the nth diffraction order can be obtained by

$$\mathbf{D}_n = \frac{1}{\Lambda}\int_0^{\Lambda}\mathbf{E}_{\text{out}}\exp(-i2\pi nx/\Lambda)\mathrm{d}x = \delta_n\cos\frac{\Gamma}{2}\begin{bmatrix} 1 \\ \pm i \end{bmatrix} - \delta_{n\pm 1}\, i\sin\frac{\Gamma}{2}\exp[\pm i(\beta\rho^3 + 2\pi\rho/d)]\begin{bmatrix} 1 \\ \mp i \end{bmatrix}. \tag{5}$$

Equations (4) and (5) show that there are only three diffraction orders for the LC CABS: the 0th order (the first term) and ±1st orders (the second term). The 0th order is the residual component with the same incident polarization state, and it can be eliminated by adjusting the phase retardation to $(2\,m + 1)\pi$ (i.e., half-wave condition, $m = 0, 1, 2\ldots$). Under this premise, when the incident polarization is LCP, the output energy will be completely diffracted to the -1st order in the RCP state. Most importantly, a positive radial cubic phase modulation referring to $+(\beta\rho^3+2\pi\rho/d)$ is achieved, indicating the generation of an inward-bending autofocusing CAB. In contrast, only the +1st LCP order appears when the input is RCP, and the corresponding negative phase modulation $-(\beta\rho^3+2\pi\rho/d)$ indicates that the generated CAB has an outward transverse acceleration [13,31], revealing an autodefocusing behavior. For any illumination of non-circular polarization, the autofocusing and autodefocusing CABs are obtained simultaneously with orthogonal circular polarization states, and the energy distribution between these two orders depends on the proportion of LCP or RCP in the input power. For example, for the linearly polarized incidence, the generated autofocusing and autodefocusing CABs possess the same diffraction efficiency (defined as the power ratio of the target order to the total input light) of 50%. Moreover, the diffraction angle or separation distance between the two orders can be adjusted by changing the period Λ. Therefore, a tunable splitter for generating and separating autofocusing and autodefocusing CABs can be demonstrated based on the LC CABS.

To realize the transfer of the designed pattern to an LC cell, a photoalignment technique based on the sulfonic azo-dye SD1 (Dai-Nippon Ink and Chemicals, Japan) is adopted [32]. The SD1 molecule orients its absorption oscillator perpendicularly to the polarization direction of the activating UV light. Moreover, owing to the rewritability of SD1, this orientation can be reconstructed by exposure to UV light with different polarization directions. When used as the alignment layer, the SD1 molecules spread their orientation to adjacent LCs by intermolecular interactions. A DMD-based (resolution 1920 × 1080; mirror pitch 10.8 μm) microlithography system (King Optronics-095A, China) equipped with a 10× objective lens [18] is employed as the exposure setup. Through an eighteen-step, five-time partly overlapping dynamic exposure process [33], the CABS pattern in Fig. 1(d) can be precisely duplicated to the LC cell, which is composed of two SD1-coated indium-tin-oxide glass substrates separated by 6-μm spacers. After the capillary filling of LC E7, a director-variant PB-phase element LC CABS can thus be formed.

3. Results and discussion

The micrograph of the LC CABS observed under an optical microscope is displayed in the inset of Fig. 2. The greenish color results from the corresponding wavelength satisfying the half-wave condition [34]. The bright areas correspond to the LC directors at ~45° or 135° to one of the crossed polarizers, and the dark areas correspond to the angles of ~0° or 90°. As the bright-to-dark pattern alternates twice as the orientation of LC directors varies from 0 to π, the microscopic image has denser fringes compared with the phase pattern in Fig. 1(d). Overall, the consecutive variations in brightness of the designed fringes confirms the accurate transfer of the PB phase pattern and the continuous orientation of the LC molecules.

As shown in Fig. 2, an optical setup is established to characterize the performance of the LC CABS. A He–Ne laser beam with wavelength of 632.8 nm in a Gaussian profile is adopted as the Gaussian light source. It passes through a polarizer and a $\lambda/4$ plate in sequence before being modulated by the LC CABS sample. The angle between the transmission direction of the polarizer and the c-axis of the $\lambda/4$ plate is set to be 45°/-45° or 0° to ensure the RCP/LCP or linear polarization incidence. A spherical lens with focal length $f_{\mathrm{L}}=10$ cm is set at a distance f_{L} from the LC sample to perform the FT. The generated autofocusing and autodefocusing CABs at different propagation distances can then be captured by a CCD (BGS-SP620, Ophir-Spiricon, USA). Herein, the focal plane of the lens (FT plane) is defined as the initial observation point (propagation distance $z=0$).

After the voltage applied to the LC CABS is adjusted to meet the half-wave condition, CABs with autofocusing and autodefocusing states can be obtained and the intensity distributions are shown in Fig. 3. As analyzed above, when the incident beam is linearly polarized, the energy is equally diffracted to the +1st LCP and -1st RCP orders, as shown in Fig. 3(a). The measured diffraction efficiency of both of these orders is ~46%, i.e., high efficiency up to 92% is achieved

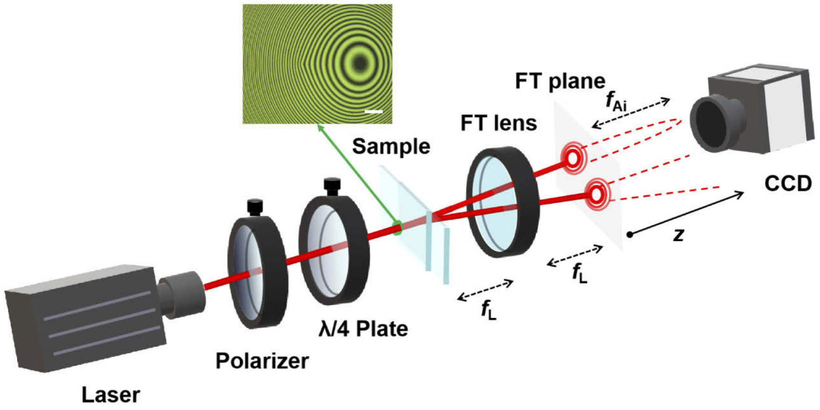

Fig. 2. Schematic diagram of the optical setup for generating, separating, and detecting autofocusing and autodefocusing CABs. The scale bar in the micrograph of the LC CABS is 100 μm.

for the conversion from a Gaussian beam to CABs. Although the intensity distributions of the two diffraction orders are almost identical at $z = 0$ (Fig. 3(a)), different propagation dynamics gradually appear with a change in z. As shown in Figs. 3(b)–3(e), captured at $z = 10$, 20, 30, and 40 cm, respectively, with increasing propagation distance the radius of the main ring of the -1st order RCP CAB decreases with increasing intensity, whereas the main ring of the +1st order LCP CAB expands with decreasing intensity, intuitively revealing an autofocusing behavior and an autodefocusing process, respectively. Herein, the generated autodefocusing CAB is different from those mentioned in Refs. [13,35,36] with ring tails distributed inside rather than outside of the main ring, which results mainly from setting the argument term of the initial radial Airy profile to be negative, i.e., $u(r) = \mathrm{Ai}[-(r_0\text{-}r)]\exp[-a(r_0\text{-}r)]$. However, it coincides well with the results proposed in Ref. [31] when the circularly symmetric beam produced via a negative linear and cubic phase modulation propagates beyond the FT plane. Under the negative phase modulation, the caustics deduced from the ray-optics experience converging before the FT lens and then diverging after passing through the lens. The diverging caustics extend up to the FT plane beyond which the wave is completely diffracted, leading to the autodefocusing behavior with the ring tails distributed outside of the main ring. This consistence also verifies the effectiveness of the geometric phase modulation represented by $-(\beta\rho^3 + 2\pi\rho/d)$. We have lowered the input power to prevent the intensity of the autofocusing CAB at the focal plane from exceeding the maximum detecting range of the CCD. Moreover, as the main ring of the CAB possesses almost half of the total energy [13], the surrounding sub-rings of the CABs at $z = 0$, as shown in Fig. 3(a), are not as obvious. However, for the autofocusing CAB, the intensity is more focused with increasing distance, leading to the appearance of the sub-rings. For better presentation and comparison, we show relatively enlarged images of the RCP autofocusing CAB and LCP autodefocusing CAB with intensity profiles in the left and right columns of Fig. 3, respectively. The images in these two columns are taken when the incidence is LCP or RCP, correspondingly, so that there is only one diffracted order. However, we still control the input power to keep the initial intensities consistent with Fig. 3(a). When the propagation distance increases to 30 cm in Fig. 3(c1), we can clearly see the main ring and sub-rings of the autofocusing CAB with intensity distributed in an exponentially decaying trend. In contrast, the rings of the autodefocusing CAB in Fig. 3(c2) are diverged to become weak such that it is difficult for the CCD to detect the intensity profile distribution. As a supplement, a simulated transverse intensity dynamics image of the autofocusing and autodefocusing CABs from $z = 0$ to the focal plane with a varying color bar is shown in Visualization 1. This vividly reveals that the two diffracted orders present opposite propagation behaviors; one converges while the other diverges. Particularly noteworthy is the fact that the closer the proximity to the focal plane, the faster the increase in intensity of the autofocusing CAB (see the changing intensity values beside the color bar), which can also be validated by the intensity profiles shown in Figs. 3(d1)–3(e1). Moreover, some ideal autofocusing CABs simulated at $z = 10$, 20, 30, and 40 cm are exhibited in Fig. 3(f). Comparing our experimental results shown in Figs. 3(a1)–3(e1) with these ideal CABs, we can see that despite the difference in the ring numbers which is inevitable due to the finite energy as a matter of fact, the intensity distribution trends, the abrupt increases in the intensity near the focal point, and the positions of the focal plane in these two sets of images basically coincide with each other, indicating a high quality generation of the CABs via the LC CABS. In addition, it is worth mentioning that despite the dispersive autodefocusing CAB rings, there is no overlap between the two orders throughout the propagating process, which is a benefit of the proper design of the phase structures shown in Fig. 1, guaranteeing a good separation effect.

Figure 4(a) exhibits the simulated side-view intensity variation of the autofocusing and autodefocusing CABs to multidimensionally show the propagation dynamics. Herein, the intensity distribution is scaled to the maximum value. It clearly reveals that the upper -1st order CAB accelerates inward in a parabolic trajectory, resulting in an autofocusing characteristic with an abrupt intensity increase at the focal plane. In comparison, the lower +1st order CAB propagates outward with decaying intensity, revealing a featured defocusing behavior. The 3D intensity dynamics of the autofocusing CAB in Fig. 4(b) better present the abruptly focused intense spot at the focus. The theoretical focal length for the autofocusing CAB is ~41.8 cm, which is calculated based on the following formula [37]:

$$f = \sqrt{\frac{48{f_L}^4\lambda^2\beta}{\pi d w^3}}, \tag{6}$$

where f_L is the focal length of the FT lens, λ is the wavelength, β is 120 for cubic phase modulation, $d = 245.7 \times 1.08$ µm $= 265.356$ µm, and $w = 1080 \times 1.08$ µm $= 1166.4$ µm is the width of the LC CABS. By measuring the radius of the main ring at different distances, we obtain the transverse accelerating dynamics of the autofocusing CAB, and the propagation trajectory is plotted in Fig. 4(c). The fitted red curves in a parabolic trend match well with the simulations as shown in Figs. 4(a) and 4(b). The measured focal length is ~40 cm, which is also quite consistent with the theoretical value considering the experimental errors. The simulations and experiments collectively verify the good performance of the LC CABS sample. It is worth mentioning that the focal length and separation distance between the autofocusing and autodefocusing CABs can be customizable, as the parameters β, d, w and Λ can be easily selected according to practical requirements. And we can also generate the CAB expressed in a more general form $u(r) = \mathrm{Ai}[(r_0\text{-}r)/w_0]\exp[a(r_0\text{-}r)/ w_0]$ (w_0 is a scaling factor) at the initial plane with any desired parameters. In this case, the radius of the primary ring and the focal length of the CAB are given by $R(0) = r_0 + w_0$ and $f_{\mathrm{Ai}} = 4\pi w^{3/2}{R_0}^{1/2}/\lambda$ [11,14], respectively. In our work, these two physical quantities are determined by $f_L\lambda/d$ (deduced from the grating diffraction formula) and Eq. (6), respectively. The apodization factor a corresponds to the cubic phase modulation parameter β. Correlating these physical quantities one to one, we can therefore generate the CAB with any desired r_0, w_0, a parameters. For example, in our work, these parameters should be 0.5303 mm, 0.0897 mm and 0.06, respectively. Besides, holography method [38] can also be adopted to generate the CAB with any desired parameters by calculating the interference of the CAB and a plane wave. However, in addition to a relatively complicated calculation process, a 4f system consisting of two lenses is usually required to filter the desired orders, leading to a bulky optical setup and lower efficiency compared with our method. Moreover, owing to the rewritability of SD1 and flexibility of the DMD-based exposure system, the LC CABS can be reconfigured

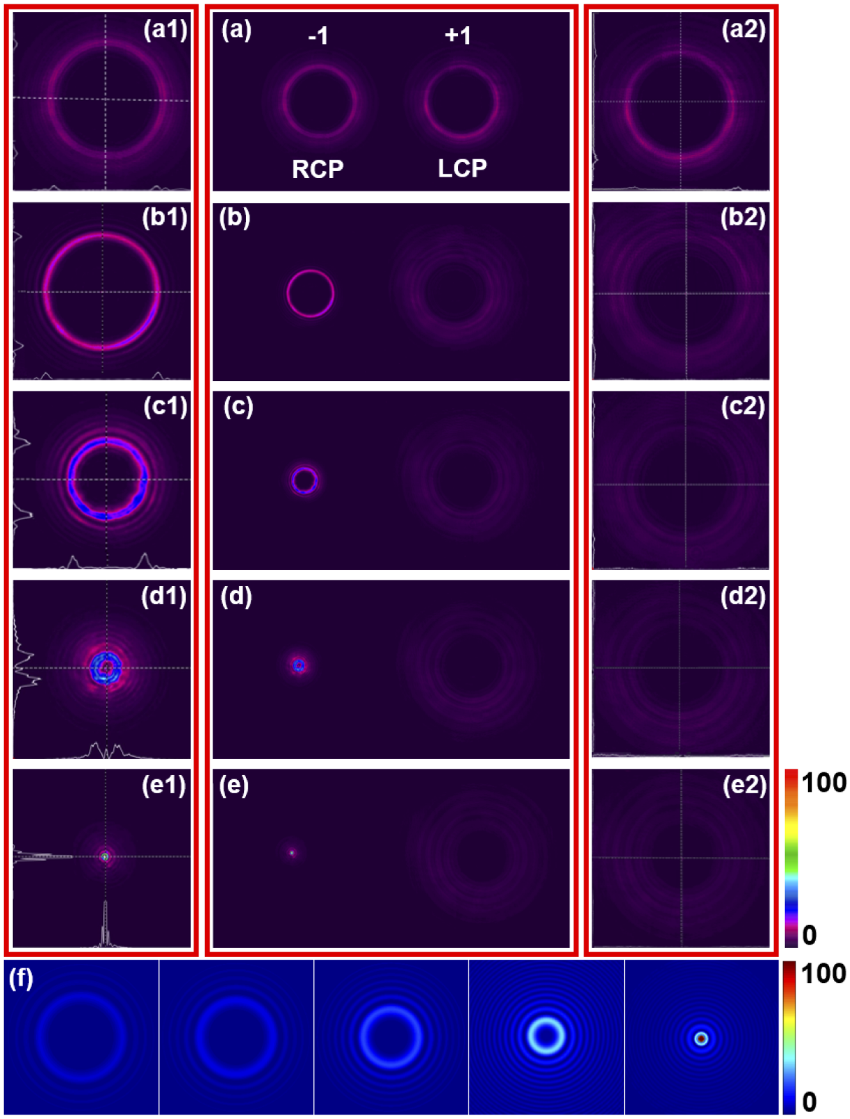

Fig. 3. Intensity distributions of the CABs at (a,a1,a2) $z = 0$ cm, (b,b1,b2) $z = 10$ cm, (c,c1,c2) $z = 20$ cm, (d,d1,d2) $z = 30$ cm, and (e,e1,e2) $z = 40$ cm, respectively. The horizontal and vertical section lines correspond to the intensity profiles. (f) Simulated ideal autofocusing CAB at $z = 0$, 10, 20, 30, and 40 cm, respectively. The intensity distribution has been scaled to the maximum.

with the newly designed phase pattern. In addition, owing to the LC property of electro-optical tunability, the working wavelength for the CABS can range from the visible to infrared or even terahertz band [34], and the switch from the generated CABs to a Gaussian beam can be achieved by simply adjusting the applied voltage to meet the full wave condition [18]. These merits provide additional advantages, such as tunability and flexibility, to the application of CABs in optics and photonics. Due to the limitation of the DMD-based exposure system, it is currently difficult to realize the manufacture of the LC CABS with larger area and simultaneously higher resolution, which restricts its application in some aspects like the generation of light bullets for long-distance propagation. Further efforts have been devoted to developing a more consummate photopatterning system with capabilities of ultrahigh resolution and large-area manufacturing.

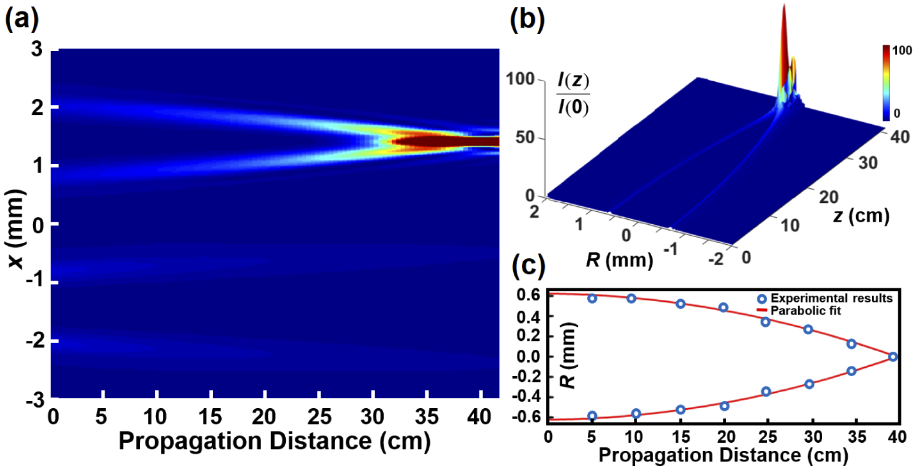

Fig. 4. (a) Simulated side-view propagation of -1st order autofocusing and +1st order autodefocusing CABs. (b) Simulated 3D propagation dynamics of the autofocusing CAB. The intensity distribution in (a) and (b) has been scaled to the maximum. (c) Experimental propagation trajectory of the autofocusing CAB. Blue circles represent the measured radius of the CAB's main ring, and the red curves are the parabolic fits.

4. Conclusion

In conclusion, we propose and demonstrate a LC CABS for the efficient generation and separation of autofocusing and autodefocusing CABs with orthogonal circular polarization states. The phase structure of the CABS is derived from the FT of a CAB combined with PB phase design. SD1-based photoalignment technology and a DMD-based microlithography system, together with a dynamic exposure method, are employed to fabricate the director-variant LC PB phase sample. The propagation dynamics of the generated autofocusing and autodefocusing CABs are revealed, and the experimental results correspond well with simulations. Moreover, the focal length and separation distance can be customized as required owing to the reconfigurability of the LC CABS. In addition, the energy distribution between the autofocusing and autodefocusing CABs and the switch between the CABs and Gaussian beam can be easily achieved by adjusting the incident polarization state or the applied voltage on the LC CABS. Furthermore, owing to the electro-optical property of LCs, the CABS sample is suitable for a wide spectral range. More research on the splitters with larger area and higher resolution is still on the way. The LC CABS is a versatile candidate for the realization of high-quality CABs with autofocusing and autodefocusing behaviors, which may promote their novel application in optical manipulation, laser nanosurgery, modern displays, and other technologies.

Funding

National Natural Science Foundation of China (11804277, 11634010, 11774289); National Key Research and Development Program of China (2017YFA0303800); Natural Science Basic Research Plan in Shaanxi Province of China (2019JQ-616); Open Foundation Project of National Laboratory of Solid State Microstructures (M31040); Open Research Fund of State Key Laboratory of Pulsed Power Laser Technology (SKL2019KF08); Fundamental Research Funds for the Central Universities (310201911cx022, 3102019JC008); Anhui Provincial Natural Science Foundation (1908085QF275).

Disclosures

The authors declare no conflicts of interest.

References

1. P. V. Loock and S. L. Braunstein, "Multipartite entanglement for continuous variables: a quantum teleportation network," Phys. Rev. Lett. **84**(15), 3482–3485 (2000).
2. F. Ferri, D. Magatti, A. Gatti, M. Bache, E. Brambilla, and L. A. Lugiato, "High-resolution ghost image and ghost diffraction experiments with thermal light," Phys. Rev. Lett. **94**(18), 183602 (2005).
3. Y. H. Lin, H. S. Chen, H. C. Lin, Y. S. Tsou, H. K. Hsu, and W. Y. Li, "Polarizer-free and fast response microlens arrays using polymer-stabilized blue phase liquid crystals," Appl. Phys. Lett. **96**(11), 113505 (2010).
4. Y. J. Wang, H. A. Hsieh, and Y. H. Lin, "Electrically tunable gradient-index lenses via nematic liquid crystals with a method of spatially extended phase distribution," Opt. Express **27**(22), 32398–32408 (2019).
5. K. Yin, Z. He, and S. T. Wu, "Reflective polarization volume lens with small f-number and large diffraction angle," Adv. Opt. Mater. **8**(11), 2000170 (2020).
6. H. S. Chen, Y. J. Wang, P. J. Chen, and Y. H. Lin, "Electrically adjustable location of a projected image in augmented reality via a liquid-crystal lens," Opt. Express **23**(22), 28154–28162 (2015).
7. Y. J. Wang and Y. H. Lin, "An optical system for augmented reality with electrically tunable optical zoom function and image registration exploiting liquid crystal lenses," Opt. Express **27**(15), 21163–21172 (2019).
8. T. Zhan, J. Zou, J. Xiong, X. Liu, H. Chen, J. Yang, S. Liu, Y. Dong, and S. T. Wu, "Practical chromatic aberration correction in virtual reality displays enabled by large-size ultra-broadband liquid crystal polymer lenses," Adv. Opt. Mater. **8**(2), 1901360 (2020).
9. Y. H. Lee, F. Peng, and S. T. Wu, "Fast-response switchable lens for 3D and wearable displays," Opt. Express **24**(2), 1668–1675 (2016).
10. T. Zhan, Y. H. Lee, and S. T. Wu, "High-resolution additive light field near-eye display by switchable Pancharatnam–Berry phase lenses," Opt. Express **26**(4), 4863–4872 (2018).
11. D. G. Papazoglou, N. K. Efremidis, D. N. Christodoulides, and S. Tzortzakis, "Observation of abruptly autofocusing waves," Opt. Lett. **36**(10), 1842–1844 (2011).
12. G. Siviloglou, J. Broky, A. Dogariu, and D. Christodoulides, "Observation of accelerating Airy beams," Phys. Rev. Lett. **99**(21), 213901 (2007).
13. P. Zhang, J. Prakash, Z. Zhang, M. S. Mills, N. K. Efremidis, D. N. Christodoulides, and Z. Chen, "Trapping and guiding microparticles with morphing autofocusing Airy beams," Opt. Lett. **36**(15), 2883–2885 (2011).
14. P. Panagiotopoulos, D. G. Papazoglou, A. Couairon, and S. Tzortzakis, "Sharply autofocused ring-Airy beams transforming into non-linear intense light bullets," Nat. Commun. **4**(1), 2622 (2013).
15. N. K. Efremidis, Z. Chen, M. Segev, and D. N. Christodoulides, "Airy beams and accelerating waves: an overview of recent advances," Optica **6**(5), 686–701 (2019).
16. T. Zhan, J. Xiong, Y. H. Lee, and S. T. Wu, "Polarization-independent Pancharatnam–Berry phase lens system," Opt. Express **26**(26), 35026–35033 (2018).
17. T. Zhan, J. Xiong, Y. H. Lee, and S. T. Wu, "Fabrication of Pancharatnam–Berry phase optical elements with highly stable polarization holography," Opt. Express **27**(3), 2632–2642 (2019).
18. B. Y. Wei, W. Hu, Y. Ming, F. Xu, S. Rubin, J. G. Wang, V. Chigrinov, and Y. Q. Lu, "Generating switchable and reconfigurable optical vortices via photopatterning of liquid crystals," Adv. Mater. **26**(10), 1590–1595 (2014).
19. I. Chremmos, P. Zhang, J. Prakash, N. K. Efremidis, D. N. Christodoulides, and Z. Chen, "Fourier-space generation of abruptly autofocusing beams and optical bottle beams," Opt. Lett. **36**(18), 3675–3677 (2011).
20. A. Chong, W. H. Renninger, D. N. Christodoulides, and F. W. Wise, "Airy-Bessel wave packets as versatile linear light bullets," Nat. Photonics **4**(2), 103–106 (2010).
21. I. Nys, K. Chen, J. Beeckman, and K. Neyts, "Periodic planar-homeotropic anchoring realized by photoalignment for stabilization of chiral superstructures," Adv. Opt. Mater. **6**(6), 1701163 (2018).
22. I. Nys, J. Beeckman, and K. Neyts, "Surface mediated alignment of long pitch chiral nematic liquid crystal structures," Adv. Opt. Mater. **6**(13), 1800070 (2018).

23. I. Nys, M. Stebryte, Y. Y. Ussembayev, J. Beeckman, and K. Neyts, “Tilted chiral liquid crystal gratings for efficient large-angle diffraction,” Adv. Opt. Mater. **7**(22), 1901364 (2019).
24. B. Y. Wei, P. Chen, W. Hu, W. Ji, L. Y. Zheng, S. J. Ge, Y. Ming, V. Chigrinov, and Y. Q. Lu, “Polarization-controllable Airy beams generated via a photoaligned director-variant liquid crystal mask,” Sci. Rep. **5**(1), 17484 (2015).
25. P. Chen, S. J. Ge, W. Duan, B. Y. Wei, G. X. Cui, W. Hu, and Y. Q. Lu, “Digitalized geometric phases for parallel optical spin and orbital angular momentum encoding,” ACS Photonics **4**(6), 1333–1338 (2017).
26. B. Y. Wei, S. Liu, P. Chen, S. X. Qi, Y. Zhang, W. Hu, Y. Q. Lu, and J. L. Zhao, “Vortex Airy beams directly generated via liquid crystal q-Airy-plates,” Appl. Phys. Lett. **112**(12), 121101 (2018).
27. P. Chen, L. L. Ma, W. Duan, J. Chen, S. J. Ge, Z. H. Zhu, M. J. Tang, R. Xu, W. Gao, T. Li, W. Hu, and Y. Q. Lu, “Digitalizing self-assembled chiral superstructures for optical vortex processing,” Adv. Mater. **30**(10), 1705865 (2018).
28. B. Wei, S. Qi, S. Liu, P. Li, Y. Zhang, L. Han, J. Zhong, W. Hu, Y. Lu, and J. Zhao, “Auto-transition of vortex- to vector-Airy beams via liquid crystal q-Airy-plates,” Opt. Express **27**(13), 18848–18857 (2019).
29. P. Chen, L. L. Ma, W. Hu, Z. X. Shen, H. K. Bisoyi, S. B. Wu, S. J. Ge, Q. Li, and Y. Q. Lu, “Chirality invertible superstructure mediated active planar optics,” Nat. Commun. **10**(1), 2518 (2019).
30. P. Chen, B. Y. Wei, W. Hu, and Y. Q. Lu, “Liquid-crystal-mediated geometric phase: from transmissive to broadband reflective planar optics,” Adv. Mater. **31**, 1903665 (2019).
31. I. D. Chremmos, Z. Chen, D. N. Christodoulides, and N. K. Efremidis, “Abruptly autofocusing and autodefocusing optical beams with arbitrary caustics,” Phys. Rev. A **85**(2), 023828 (2012).
32. H. Akiyama, T. Kawara, H. Takada, H. Takatsu, V. Chigrinov, E. Prudnikova, V. Kozenkov, and H. Kwok, “Synthesis and properties of azo dye aligning layers for liquid crystal cells,” Liq. Cryst. **29**(10), 1321–1327 (2002).
33. P. Chen, B. Y. Wei, W. Ji, S. J. Ge, W. Hu, F. Xu, V. Chigrinov, and Y. Q. Lu, “Arbitrary and reconfigurable optical vortex generation: a high-efficiency technique using director-varying liquid crystal fork gratings,” Photonics Res. **3**(4), 133–139 (2015).
34. B. Y. Wei, P. Chen, S. J. Ge, L. C. Zhang, W. Hu, and Y. Q. Lu, “Liquid crystal depolarizer based on photoalignment technology,” Photonics Res. **4**(2), 70–73 (2016).
35. C. Y. Hwang, K. Y. Kim, and B. Lee, “Bessel-like beam generation by superposing multiple Airy beams,” Opt. Express **19**(8), 7356–7364 (2011).
36. D. Mansour and D. G. Papazoglou, “Tailoring the focal region of abruptly autofocusing and autodefocusing ring-Airy beams,” OSA Continuum **1**(1), 104–115 (2018).
37. J. A. Davis, D. M. Cottrell, and D. Sand, “Abruptly autofocusing vortex beams,” Opt. Express **20**(12), 13302–13310 (2012).
38. S. Liu, M. Wang, P. Li, P. Zhang, and J. Zhao, “Abrupt polarization transition of vector autofocusing Airy beams,” Opt. Lett. **38**(14), 2416–2418 (2013).